Controlling Structure and Function of Polymeric Drug Delivery Nanoparticles Using Microfluidics

Aman Bains, Yimeng Cao, Sundiata Kly, Jeremy E. Wulff, & Matthew G. Moffitt

May 2017

Controlling Structure and Function of Polymeric Drug Delivery Nanoparticles Using Microfluidics

Aman Bains, Yimeng Cao, Sundiata Kly, Jeremy E. Wulff, and Matthew G. Moffitt*

Department of Chemistry, University of Victoria, P.O. Box 3065, Victoria, BC, Canada V8W 3V6

Abstract

We demonstrate control of multiscale structure and drug delivery function for paclitaxel (PAX)-loaded polycaprolactone-*block*-poly(ethylene oxide) (PCL-*b*-PEO) polymeric nanoparticles (PNPs) *via* synthesis and flow-directed shear processing in a two-phase gas-liquid microfluidic reactor. This strategy takes a page from the engineering of commodity plastics, where processing rather than polymer chemistry provides an experimental handle on properties and function. PNPs formed from copolymers with three different PCL block lengths show sizes, morphologies, and loading efficiencies that depend on both the PCL block length and the microfluidic flow rate. By varying flow rate and comparing with a conventional bulk method of PNP preparation, we show that flow-variable shear processing provides control of PNP sizes and morphologies and enables slower PAX release times (up to 2 weeks) compared to bulk-prepared PNPs. Antiproliferative effects against cultured MCF-7 breast cancer cells were greatest for PNPs formed at an intermediate flow rate, corresponding to small and low-polydispersity spheres formed uniquely at this flow condition. Formation and flow-directed nanoscale shear processing in gas-liquid microfluidic reactors provides a manufacturing platform for drug delivery PNPs that could enable more effective and selective nanomedicines through multiscale structural control.

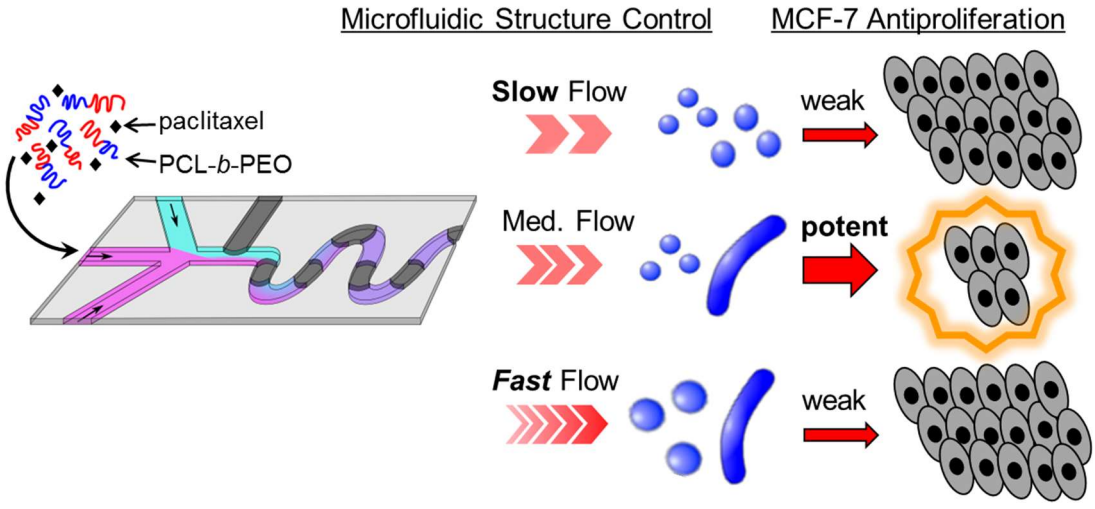

Introduction

Polymeric nanoparticles (PNPs) for drug delivery have received increasing attention due to their morphological variability, robustness, and ease of functionalization.[1-20] For example, micellar aggregates of biocompatible and biodegradable block copolymers,[21-26] including poly(ε-caprolactone)-*block*-poly(ethylene oxide) (PCL-*b*-PEO),[22,27-37] have been used to encapsulate a wide range of hydrophobic drugs in order to enhance bioavailability and selectively. Numerous efforts toward improved drug delivery systems have focused on controlling the chemistry of PNPs through polymer synthesis or modification.[10,11,13-17,38-41] For example, the hydrophobic PNP core can be modified with pendant chains or functional groups to improve encapsulation of specific drugs,[14,15] or reversible bonds or crosslinks can be added to trigger site-specific release inside a cancer cell;[11,17,39,40] also, the hydrophilic shell can be functionalized with various ligands (including antibodies and proteins) to induce active targeting through site-specific binding to cancer cells.[10,11,13,16,17,38,41]

In addition to such critical roles of PNP *chemistry*, the importance of PNP *structure* for drug delivery function is increasingly recognized.[16,26,33,36,42-50] For example, on the colloidal scale (~10-100 nm), PNP sizes and morphologies are critical factors influencing biodistributions, circulation times, and cellular uptake;[26,42-45,47] on the nanoscale (~1-10 nm), the crystallization of hydrophobic chains can strongly affect PNP stabilities, flexibilities, and drug release rates.[16,33,36,48-50] Considering these complex and multiscale relations between PNP structure and therapeutic function, manufacturing approaches offering continuous and convenient variability of structure on multiple length scales should provide more effective routes to optimizing polymeric nanomedicines.

Conventional synthetic methods for block copolymer PNPs employ intermolecular "bottom-up" forces, requiring variations in the chemistry of the formulation— including block copolymer composition,[51,52] solvent,[53] or acid/salt additives[54,55]— in order to modulate PNP structure. An entirely different approach is to apply variable shear as an external or "top-down" force,[56,57] enabling tuning of PNP multiscale structure and function without the need for changing the polymer or other formulation components. This potentially transformative route is inspired by the engineering of commodity polymeric materials, where polymer processing rather than polymer chemistry provides an engineering handle on the final material properties (for example, the stretching of extruded nylon fiber to improve their sheen and tensile strength, known as "cold drawing").[58] However, a critical difference between process engineering of commodity plastics and drug delivery PNPs is that, in the latter case, shear processing requires velocity gradients acting over colloidal dimensions, representing shear rates orders of magnitude higher than are typical in commercial polymer processing methods such as extrusion and injection molding.[58] Operating under the macroscopic volumes and dimensions of conventional PNP preparations, such shear rates are inaccessible without impractical energy costs; for this reason, the application of shear processing to control the structure and properties of drug delivery PNPs has not been previously demonstrated to our knowledge.

Recent developments in manufacturing PNPs using microfluidics have been spurred by the potential for fast and efficient on-chip screening and fine control of reagent concentrations.[12,59-61] Although numerous strategies for microfluidic mixing have been developed, very few microfluidic platforms for PNP production have been shown to exhibit strong shear effects.[62] Our group has recently demonstrated that two-phase gas-liquid microfluidic reactors provide a unique platform for self-assembly and processing control of PNP

sizes, morphologies, and polydispersities, due to localized regions of extreme shear ("hot spots") in which maximum shear rates (~10^5-10^6 s^{-1}) can be continuously varied *via* changes in flow rate.[56,57,63-66] In a recent study, we employed the shear processing capabilities of this reactor to produce PCL-*b*-PEO PNPs with flow-variable sizes, morphologies, and PCL crystallinities.[67,68] As a proof-of-concept, we tested the reactor for loading paclitaxel (PAX) into the PNPs at low (non-therapeutic) levels (< 0.01 encapsulated drug/polymer, w/w), demonstrating that flow rate in the microchannels provides an experimental handle on loading efficiencies and release kinetics.[67] Those preliminary results highlighted the potential of the two-phase microfluidics platform for producing drug delivery PNPs with continuously variable, flow-controlled multiscale structure and therapeutic function.

In this work, we demonstrate that manufacturing and flow-variable shear processing of PAX-loaded PNPs in a two-phase gas-liquid microfluidic reactor provides top-down control of multiscale structure and concomitant tuning of important figures of merit for therapeutic function, including loading levels, *in vitro* release profiles and MCF-7 antiproliferative effects. We show that the top-down handle of variable flow rate enables the preparation of smaller and less size-disperse particles with slower release kinetics and higher MCF-7 toxicity than can be achieved using conventional non-microfluidic approaches to PNP formulation. As a platform for screening and manufacturing polymeric nanomedicines, gas-liquid microfluidic reactors offer a new dimension in particle control *via* flow-directed processing at the nanoscale, opening new routes to higher selectivity, better targeting, and increased efficacy of drug delivery formulations.

Experimental

Materials. Three different poly(ε-caprolactone)-*block*-poly(ethylene oxide) (PCL-*b*-PEO) copolymers with constant PEO block length and variable PCL block lengths were purchased from Advanced Polymer Inc. and used as received: PCL_{12k}-*b*-PEO_{5k}; $PCL_{6.4k}$-*b*-PEO_{5k}; $PCL_{2.1k}$-*b*-PEO_{5k}, where numbers in subscripts refer to number-average molecular weights of the respective blocks; these three copolymers are referred to simply as PCL12k, PCL6.4k and PCL2.1k throughout the paper. *N,N*-dimethylformamide (DMF) (Aldrich, 99.9+%, HPLC grade, H_2O < 0.03%), paclitaxel (PAX, Polymed Therapeutics, Inc.), methyl *tert*-butyl ether (Sigma-Aldrich) and bovine serum albumin (Sigma Aldrich), were used as received without further purification. The MCF-7 (human adenocarcinoma breast cancer) cell line was obtained as a generous gift from the BC Cancer agency. The CellTiter-Blue Cell Viability Assay kit (Promega) was used according to the manufacturer's instructions. Antiproliferative assays were conducted using pre-sterilized 96-well flat-bottomed plates from BD Falcon.

Quantitative stock solutions of PCL-*b*-PEO in DMF or PCL-*b*-PEO and PAX in DMF were prepared gravimetrically by accurately weighing the solid(s) into clean glass vials followed by gravimetric addition of a known quantity of DMF; all stock solutions were equilibrated overnight with stirring before further use.

Critical Water Content Determination. Static light scattering (SLS) measurements were carried out to accurately determine the critical water content (cwc) of 0.33 wt % DMF solutions of PCL-*b*-PEO, which was the initial condition for all self-assembly experiments in this study. SLS measurements were carried out using a Brookhaven Instruments photon correlation

spectrometer equipped with a BI-200SM goniometer, a BI-9000AT digital autocorrelator, and a Melles Griot He-Ne Laser (633 nm) with a maximum power output of 75 mW.

A 1.0 wt % stock solution of PCL-*b*-PEO in DMF was filtered through a Teflon syringe membrane filter with a nominal pore size of 0.45 μm (VWR) into precleaned scintillation vials. The filtered stock was diluted to 0.33 wt % by gravimetric addition of the required quantity of DMF. To the resulting ~6 g of solution, deionized water was added in successive 0.03-0.06 g quantities via a microsyringe equipped with two membrane filters (VWR) with nominal pore size of 0.20 μm connected in series. After each addition of water, the solution was agitated using a vortexer to aid in mixing. The solution was then allowed to equilibrate for 15 min before measuring the scattered light intensity. All measurements were carried out at a scattering angle of 90° and a temperature of 23 °C. From the resulting plot of scattered light intensity versus weight percentage of added water, the cwc was determined from the intercept of linear fits to the baseline and the region of the plot in which scattered light intensity increased sharply, as described in ref. 67. Determinations of cwc were carried out three times for each copolymer from the same stock solution and the mean value and standard deviation of the three measurements were used to calculate the reported cwc values (Table S1) and experimental errors.

Microfluidic Chip Fabrication. Negative masters were fabricated on high quality silicon wafers (Silicon Quest International, Santa Clara, CA) using the negative photoresist SU-8 100 (Microchem Inc.). Immediately prior to use, the wafers were heated on a hot plate at 200 °C for 20 minutes to remove moisture. A 150 μm-thick SU-8 film was spin-coated onto the silicon and then heated to 95 °C for 60 minutes to remove residual SU-8 solvent. A photomask was then placed over the SU-8 film and exposed to UV light for 180 s. Then, the UV-treated film was

heated at 95 °C for 20 min before submersion in SU-8 developer (Microchem) until all unexposed photoresist was removed.

Microfluidics chips were fabricated from poly(dimethylsiloxane) (PDMS) using a SYLGARD 184 silicon elastomer kit (Dow Corning, Midland, MI). To optimize adhesion between the channel and substrate PDMS layers, elastomer base-to-curing agent ratios of 7:1 and 20:1 were used for the two layers, respectively. For fabrication of all PDMS chips, the elastomer and curing agent were mixed together and degassed in a vacuum chamber. The degassed PDMS was then poured over the negative master in a Petri dish and further degassed until all remaining air bubbles were removed. The PDMS was then heated at 85 °C for ~60 min until cured. The microfluidic chip was then peeled off of the negative master and holes were punched through its reservoirs to allow for the insertion of tubing. A thin PDMS film (substrate layer) was also formed on a glass slide by spin-coating and was permanently bonded to the base of the microfluidic reactor (channel layer) after both components were exposed to oxygen plasma for 60 s. The reactor has a set channel depth of 150 μm and consists of a sinusoidal mixing channel 100 μm wide and 18 mm in length and a sinusoidal processing channel 200 μm wide and 740 mm in length (Figure 1).

For stabilization of the bubble generation process, an external resistor chip was connected between the Ar gas tank and the microfluidic chip. The resistor chip effectively dampened pressure fluctuations caused by the Ar gas tank and the bubble generation process. The total pressure drop in the external resistor chip was at least one order of magnitude higher than the pressure drop in the reaction channel. The resistor chip channels were 1000 mm long, 150 μm deep and 400 μm wide.

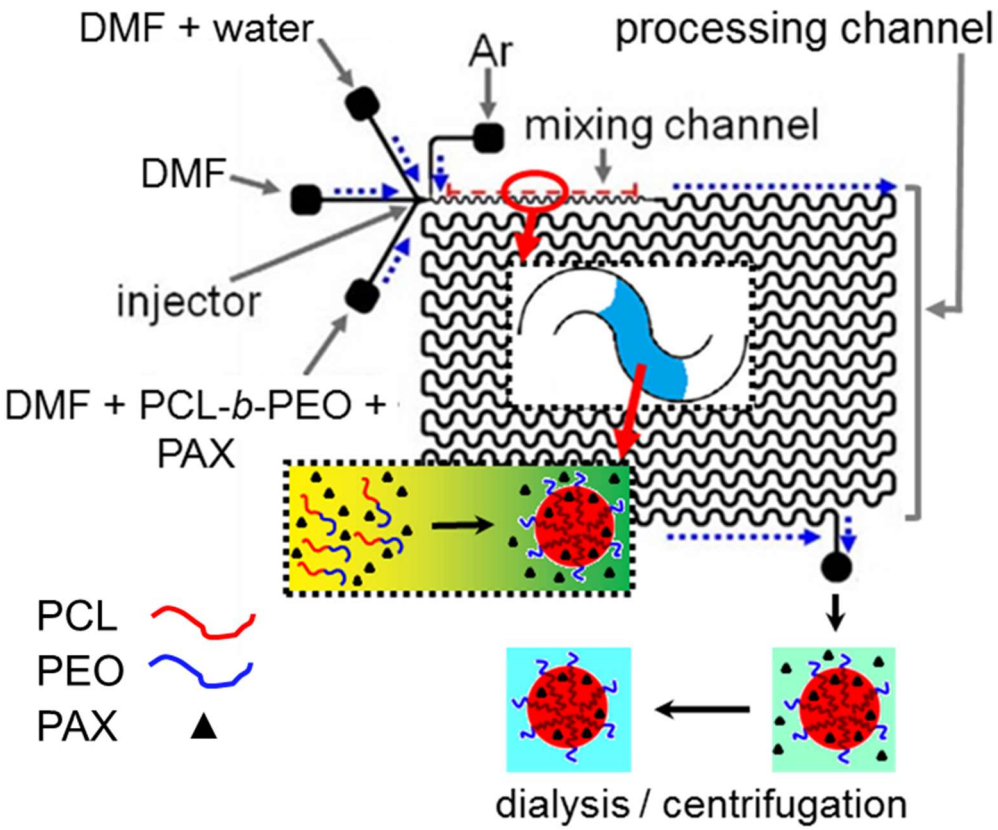

Figure 1. Schematic describing two-phase gas-liquid microfluidic reactor and microfluidic PNP preparation.

Flow Delivery and Control. Pressure-driven flow of liquids to the reactor inlet was provided using 1 mL gastight syringes (Hamilton, Reno, NV) mounted on syringe pumps (Harvard Apparatus, Holliston, MA). The microchip was connected to the liquid syringes via 1/16th-inch (OD) Teflon tubing (Scientific Products and Equipment, ON). Gas flow was introduced to the microchip via an Ar tank regulator and a downstream regulator (Johnston Controls) for fine adjustments. The microchip was connected to the regulator and resistor chip through a 1/16th-inch (OD) / 100-μm (ID) Teflon tube (Upchurch Scientific, Oak Harbor, WA). The liquid flow rate (Q_{liq}) was programmed via the syringe pumps and the gas flow rate (Q_{gas}) was fine-tuned via the downstream pressure regulator in order to dial in the nominal total flow

rates (denoted Q) described in the main text. Due to the compressible nature of the gas and the high gas/liquid interfacial tension, discrepancies arise between the nominal (programmed) and actual values of Q_{gas}, Q_{gas}/Q_{liq}, and the total flow rate (Q_{total}). Therefore, actual gas flow rates (Tables S2 and S3) were calculated from the frequency of bubble formation and the average volume of gas bubbles, determined from image analysis of the mean lengths of liquid and gas plugs, L_{liq} and L_{gas}, respectively, under a given set of flow conditions. This method of flow calculation has been previously employed in the context of gas-liquid segmented flow in the microfluidic device. For all experiments, the relative gas-to-liquid flow ratio, Q_{gas}/Q_{liq} ~1 and all actual Q_{total} values are within 10% of nominal Q values reported in the main text.

Visualization of the gas bubbles and liquid plugs within the microfluidic reactor was achieved using an upright optical microscope (Omax) with a 10×-objective lens. Images were captured using a 2.07 megapixel PupilCam (Ken-A-Vision) and mean lengths of liquid and gas plugs were determined from the images using image analysis software (ImageJ).

Microfluidic Preparation of PAX-Loaded PNPs. Various PAX-loaded PNP samples were prepared by combining three fluid streams at equal flow rate to form gas-segmented liquid plugs within the reactor: (1) a DMF solution containing 1 wt % PCL2.1k, PCL6.4k, or PCL12k with codissolved PAX in a drug : polymer ratio (w/w) of r = 0.1, 0.25, 0.5, or 0.6; (2) a separator stream containing DMF only; and (3) a DMF solution containing deionized water at concentrations of 54.3, 33.9 or 31.5 wt % for PCL2.1k, PCL6.4k, and PCL12k samples, respectively. In all cases, combination of the three liquid streams yielded steady-state concentrations of 0.33 wt % copolymer; steady-state water concentrations for each copolymer were selected such that water contents relative to the critical value were cwc + 5.0 wt % in all cases.

The PAX-loaded PNP samples were collected from the reactor into vials containing a 10×-excess volume of deionized water, followed by 12 h dialysis against deionized water (with changing of water every hour for the first 4 h of dialysis) to remove residual DMF. Then, aqueous PNP dispersions were centrifuged at 12,000 × g to remove precipitated unencapsulated PAX. All samples were prepared in triplicate from separately prepared stock solutions under the specified conditions.

Bulk Preparation of PAX-Loaded PNPs. Selected PAX-loaded PNP samples were also prepared by a conventional drop-wise water addition method for comparison with microfluidic preparations ("bulk" preparation method). Initial conditions for self-assembly were kept identical to the on-chip formulations. Thus, to ~5 mL of a 0.33 wt % copolymer solution in DMF with codissolved PAX, water was added drop-wise using a micropipette at a constant rate of 20 μL every 10 s with moderate magnetic stirring (600 RPM). Drop-wise water addition at constant rate was continued to a water content of 80 wt %, then the PNPs were quenched immediately into

10×-volume excess of deionized water, followed by 12 h dialysis against deionized water (with changing of water every hour for the first 4 h of dialysis) to remove residual DMF. Then, aqueous PNP dispersions were centrifuged at 12,000 × g to remove precipitated unencapsulated PAX. All samples were prepared in triplicate under the specified conditions.

Transmission Electron Microscopy. Transmission electron microscopy (TEM) was performed using a JEOL JEM-1400 TEM, operating at an accelerating voltage of 65 kV and equipped with a Gatan Orius SC1000 CCD camera. TEM images were obtained by depositing diluted dispersions (~0.03 wt % copolymer) consisting of PAX-loaded PCL-*b*-PEO PNPs in water onto carbon-coated 300 mesh copper TEM grids as described below.

To improve contrast, uranyl acetate was used to negatively stain the PCL-*b*-PEO PNPs. Uranyl acetate selectively binds to the PEO coronal chains, providing reverse contrast for the PCL cores, which appear white in TEM images of stained samples. For reverse staining experiments, PNP dispersions were mixed with 1 wt % aqueous solution of uranyl acetate in a 1:1 ratio (v/v) and one drop of the resulting mixture was deposited onto a TEM grid. Excess liquid was immediately removed using lens paper, followed by drying of remaining liquid under ambient conditions. For each set of conditions, reported prominent morphologies were determined from TEM analysis of three separate preparations. For each sample preparation, at least 2-3 TEM images taken in different regions of the grid were evaluated. To distinguish spherical PNPs from vesicles, TEM images of selected samples without negative staining were also obtained (Supporting Information, Figure S6).

Dynamic Light Scattering. Hydrodynamic diameter distributions were determined using dynamic light scattering (DLS). DLS measurements were carried out using a Brookhaven

Instruments photon correlation spectrometer equipped with a BI-200SM goniometer, a BI-9000AT digital autocorrelator, and a Melles Griot He-Ne Laser (633 nm) with a maximum power output of 75 mW. All DLS measurements were performed in pure water at 23˚C and a scattering angle of 90˚.

PAX-loaded PNPs were transferred to pre-cleaned scintillation vials then diluted 5× using deionized water that had been filtered through two nylon syringe filters in series with nominal pore sizes of 0.2 m (National Scientific Company) to give a final copolymer concentration of ~0.07 mg/mL Scattering intensity-weighted size distributions were determined from CONTIN analysis.

X-Ray Diffraction. X-ray diffraction (XRD) measurements were performed on a Rigaku Miniflex diffractometer with a Cr source (kR radiation, λ = 2.2890 Å) operating at 30 kV and 15 mA with a resolution of 0.05° (2θ) and a scan speed of 1°/min. X-ray diffraction profiles were collected for 2θ ranging from 10-80 degrees. For XRD sample preparation, water was removed from suspensions of PAX-loaded PNPs by rotory evaporation at 25 °C until solid films were obtained. The resulting films were then scraped as a powder into the XRD specimen holder with no subsequent drying step.

Peak deconvolution of XRD data was done using Origin Pro Version 8.1 as described in ref. 67. Briefly, XRD data were fit to a sum of 6 Lorentzian functions: 3 peaks assigned to crystalline PCL (2θ = 32.5°, 32.7°, and 35.7°), 2 peaks assigned to crystalline PEO (2θ = 29.2° and 35.4°), and 1 peak (no fixed position) assigned to incoherent scattering from amorphous copolymer (amorphous halo). Areal peak contributions from the three components (crystalline

PCL, crystalline PEO, and amorphous copolymer) were then determined by integration and the percentage of crystalline PCL, χ_{PCL}, was calculated using:

$$\chi_{PCL} = (A_{PCL}/A_{total}) \times 100\ \%$$

where $A_{total} = A_{PCL} + A_{PEO} + A_{amorph.}$

PAX Loading Efficiency Determination. To determine PAX loading efficiencies, water was removed from a known mass (~1 g) of an aqueous PNP dispersion by rotary evaporation at 25 °C. Then a known amount (~0.5 g) of acetonitrile (ACN) was added to break up the PAX-loaded PNPs by stirring in ACN for 4 h. PAX quantification was conducted using high performance liquid chromotography (HPLC, Ultimate 3000, Thermo Scientific) with a C18 column (Phenomenex Luna 5u C18) and a mobile phase composition of 65/35 ACN/water (v/v) + 1 vol % formic acid, coupled to a diode array detector (DAD) operating at a characteristic absorption wavelength of 227 nm. Sample injection volumes were 50 μL and the HPLC-MS flow rate was set to 1 mL/min. A calibration curve for the DAD was generated by analysis of 5 stock solutions containing different known PAX concentrations in ACN. Quantities of PAX in the various dispersions were determined and loading efficiencies calculated for each sample using:

$$loading\ efficiency\ (\%) = \frac{mass\ of\ encapsulated\ PAX\ (g)}{total\ mass\ of\ PAX\ (g)} \times 100$$

Reported loading efficiencies and loading levels are averages determined from triplicate PNP preparations under the specified conditions. The loading level of a PNP preparation is defined as the following ratio:

$$loading\ level = \frac{mass\ of\ encapsulated\ PAX\ (g)}{mass\ of\ copolymer\ (g)}$$

Loading levels are determined from the loading ratio, *r*, and the loading efficiency as follows:

$$loading\ level = r \times \frac{loading\ efficiency}{100}$$

Where *r* is the following ratio:

$$loading\ ratio, r = \frac{total\ mass\ of\ PAX\ (g)}{mass\ of\ copolymer\ (g)}$$

***In Vitro* PAX Release Kinetics.** Experiments were carried out to monitor the *in vitro* release of PAX from PAX-loaded PNPs using high performance liquid chromatography-mass spectrometry (HPLC-MS, Ultimate 3000, Thermo Scientific) with a C18 column (Phenomenex Luna 5u C18) and a mobile phase composition of 65/35 ACN/water (v/v) + 1 vol % formic acid. In a typical experiment, ~10 g of aqueous dispersion of PAX-loaded PNPs were transferred to a 10 mL-dialysis bag (SpectrumLabs, MWCO 100 kDa) which was placed in a 4 L-beaker of the release medium, consisting of ~2.5 L of a 1% phosphate buffer saline (PBS, pH = 7.4) solution containing albumin (Sigma Aldrich) at a concentration of 45 g/L; throughout release experiments, the release medium was constantly stirred using magnetic stirring and maintained at physiological temperature (37 °C) in an incubator.

At each predetermined time, an aliquot of known mass (~1 g) was removed from the dialysis bag to which a known mass (~150 mg) of a deuterated PAX internal standard (d5-PAX, ~1 mg/mL, Toronto Research Chemicals) in ACN was added. A liquid-liquid extraction was conducted using methyl tert-butyl ether (Sigma Aldrich). The top organic liquid phase containing PAX and internal standard was decanted from the lower aqueous phase containing albumin. The methyl tert-butyl ether was then removed by rotary evaporation at 25 °C then a known quantity of ACN (0.1-0.5 g depending on release time) was added. The resulting solution was injected

into the HPLC-MS and PAX and d5-PAX were detected and quantified using the MS detector by single ion monitoring (SIM) of the m/z = 286 and m/z = 291 peaks, respectively. Separate calibration curves for SIM detection of PAX and the internal standard were generated by analysis of five known stock solutions of both analytes. The internal standard (d_5-PAX) was used to determine the efficiency of each liquid-liquid PAX extraction, which was found to vary from 60-80%. These extraction efficiencies were used to calculate PAX concentrations in each aliquot before liquid-liquid extraction from PAX concentrations determined by HPLC-MS. From determined masses of PAX in aliquots obtained at different release times, percentages of PAX released were calculated relative to the determined mass of PNP-encapsulated PAX at the $t = 0$ release time. Reported release percentages at each release time are averages determined from triplicate PNP preparations under the specified conditions.

Cell-Culture and Antiproliferation Assay. MCF-7 cells were grown to ~95% confluence in Dulbecco's Modified Eagle's Medium (DMEM) supplemented with 10% fetal bovine serum (FBS) in a 75 cm^2 tissue culture flask and maintained at 37 °C with 5% CO_2 in a tissue culture incubator. Cells were then trypsinized, collected and pelleted by centrifugation (3 minutes at 160 × g. The cell pellet was then resuspended in DMEM media and the cell concentration was determined using a hemocytometer. After the initial cell concentration was determined the suspension was diluted to 1.0×10^5 cells/mL. Next, a multichannel pipet was used to fill a 96 well plate with 100 µL/ well of the diluted cell suspension. The cell loaded plates were then incubated for 24 h at 37 °C under an atmosphere of 5% CO_2.

According to calculated loading levels, aqueous stock dispersions of each investigated sample of PAX-loaded PNPs were prepared by either diluting or concentrating the original dispersions, such that 100× dilution of the stock would result in a working PAX concentration of

2 μg/mL. After 24 hours cell incubation, 6.5 μL aliquots of stock dispersions of aqueous PAX-loaded PCL-*b*-PEO PNPs or 6.5 μL of free PAX dissolved in dimethylsulfoxide (DMSO) were diluted in 643.5 μL of DMEM media to obtain a working PAX concentration of 2 μg/mL. Serial dilutions were carried out, and then 100 μL of each diluted stock was added to the appropriate well of the 96-well plate (containing ~1.0×10^4 cells in 100 μL of media, as described above), in order to generate a range of different concentrations for analysis (1, 0.308, 0.095, 0.029, 0.0090, 0.0028, 8.5×10^{-4}, and 2.6×10^{-4} μg/mL PAX). The treated cells were incubated for 48, 72 or 96 hours at 37 °C under a 5% CO_2 atmosphere. In order to determine cell viability, 20 μL of CellTiter-Blue was added to each well after the predetermined incubation time was complete. After the addition of the CellTiter-Blue the 96 well plates were incubated for 4 hours (5% CO_2, 37 °C) and then fluorescence (λ_{ex} = 560 nm; λ_{em} = 590 nm emission) readings were recorded on a 96-well plate reader. Percent Growth was calculated for each well, based upon the following formula:

$$\%\, Growth = 100 \times \frac{(S - B_o)}{(B_t - B_o)}$$

where S is the sample reading (cells + drug + media), B_t is the average reading for the untreated population of cells (cells + media), and B_0 is the average reading of untreated population of cells at the beginning of the experiment (cells + media at t = 0). In the above equation, the numerator represents cell proliferation in the presence of drug and the denominator represents cell proliferation in the absence of drug. Percentage Growth data sets were fit using XLfit (IDBS) and by forcing fits through 100 % growth at low PAX concentrations. Reported GI_{50} values were determined from three separate nanoparticle preparations, with each concentration of each preparation being tested 18 times (see Figures S2-S4 for complete plots of Percentage Growth

and fits). Standard errors (reported numerically in Table 3, and used as error bars in Figure 6) were obtained from the goodness of fit for each GI_{50} plot, using the statistical package in XLfit. These same standard errors were then used to calculate the *p*-values used to determine statistical significance for comparisons between measured growth inhibition results.

Results and Discussion

Effect of PCL Block Length on Microfluidic-Prepared Drug Delivery PNPs. We first studied the effect of PCL block length on PAX-loaded PNPs prepared in the microfluidic reactor. For these experiments, the loading ratio *r* was held constant at the lowest investigated value of *r* = 0.10. Table 1 summarizes the resulting PNP characteristics (morphologies, hydrodynamic sphere diameters, PCL crystallinities, and loading efficiencies/levels) from triplicate preparations under each set of conditions.

Table 1. Characteristics of PAX-Loaded PNPs Described in Figures 2 and 3.

Copolymer	*Q* (μL/min)	*r*	Morphologies[a]	χ_{PCL} (%)	Loading Efficiency (%)	Loading Level[b]
PCL(2.1k)	100	0.10	S (13), RC, L	4 ± 1	8 ± 2	0.008 ± 0.002
	200	0.10	V, S (11), L	7 ± 2	26 ± 4	0.026 ± 0.004
PCL(6.4k)	100	0.10	S (28), C, L	11 ± 2	9 ± 3	0.009 ± 0.003
	200	0.10	S (35), C, L	16 ± 4	28 ± 4	0.028 ± 0.004
PCL(12k)	100	0.10	S (23), L	18 ± 3	36 ± 8	0.036 ± 0.008
	200	0.10	V, S (30), C, L	26 ± 5	26 ± 4	0.026 ± 0.004

a) Prominent morphologies are indicated as S (spheres), C (cylinders or filomicelles), RC (rigid cylinders), V (vesicles), and L (lamellae). Numbers in brackets indicate peak hydrodynamic diameters (in nm) of spheres (assumed to be smallest-sized population) from CONTIN analysis.

b) Calculated from *loading level* = (*r* × *loading efficiency*) / 100

Figure 2 shows representative TEM images and associated intensity-weighted DLS hydrodynamic size distributions of PAX-loaded PNPs formed from PCL2.1k, PCL6.4k, and PCL12k at two different flow rates (Q = 100 and 200 μL / min). The DLS CONTIN results are more representative of colloidal sizes (including the solvated PEO layer) and overall population distributions than the associated individual TEM images; therefore TEM images were used to assess morphologies while DLS was used to compare the hydrodynamic sizes of spheres (assumed to be the smallest-sized peak in the CONTIN distribution) in the various samples. All preparations show a mixture of small spheres (insets) along with larger aggregates of various morphologies (lamellae, rigid cylinders, long filaments, and vesicles). TEM and DLS data indicate clear differences in morphologies and particle sizes as the length of the PCL block increases at a constant flow rate of Q = 100 μL / min (Figure 2, A-C). An increase in flow rate from Q = 100 μL / min to Q = 200 μL / min leads to an increase in the maximum shear rate within the channels, triggering changes in PNP sizes and morphologies (Figure 2, D-F) and PCL crystallinities (Table 1) *via* coupling of bottom-up (intermolecular) forces and top-down (shear) forces. For example, a marked increase in filament PNPs from PCL 6.4k is found at the higher flow rate (Figure 2, B and E); in the PCL12k case, vesicles are formed at Q = 200 μL / min (Figure 2F) which are not observed from PNP formation at Q = 100 μL / min (Figure 2C).

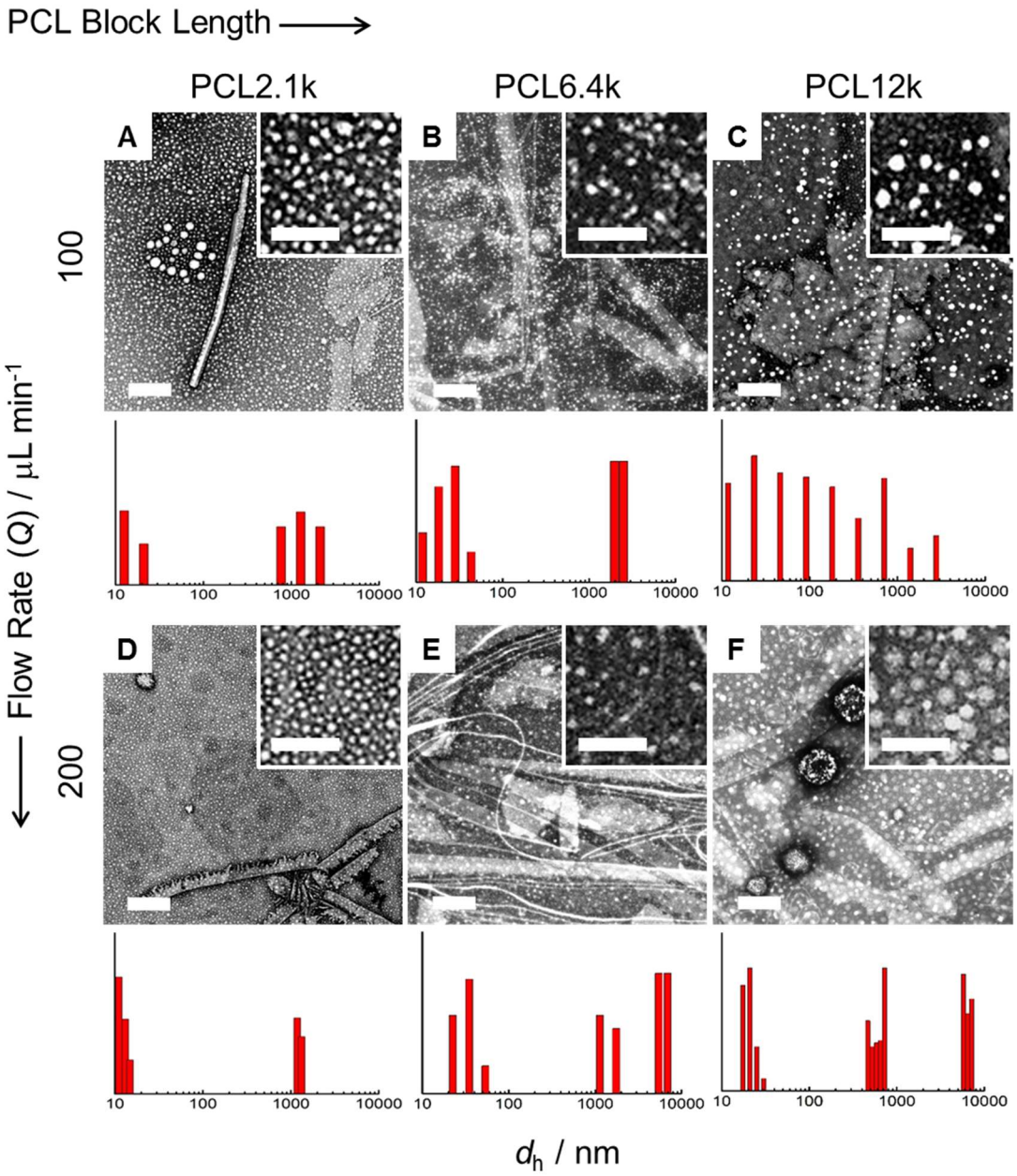

Figure 2. Effect of PCL block length on morphologies and sizes of PAX-loaded PNPs prepared in the microfluidic reactor at two different flow rates. Representative TEM images and DLS CONTIN size distributions for PNPs formed from PCL2.1k (A, D), PCL6.4k (B, E), and PCL12k (C, F) at flow rates for Q = 100 μL / min (A-C) and Q = 200 μL / min (D-F). For these experiments, the loading ratio was r = 0.10. All scale bars are 200 nm.

Flow rate also appears to provide an experimental handle on PAX loading efficiencies (Figure 3), which increase with an increase in flow rate in the cases of PCL2.1k and PCL6.4k.

This is attributed to the corresponding formation of morphologies with larger core volumes (e.g. long filaments in the PCL6.4k case) which better solubilize hydrophobic molecules.[15,16] In contrast, the loading efficiency of PCL12k is relatively high at Q = 100 µL / min and decreases with the increase in flow rate. We attribute this trend to an increase in shear-induced PCL crystallization with flow rate (Table 1). PCL crystallinity will impede encapsulation of hydrophobic cargo, which is solubilized in amorphous PCL regions.[67] The higher volume of crystallites in the PNP cores of PCL12k will exclude more PAX than in the PCL2.1k and PCL6.4k cases, explaining the observed drop in loading efficiency for PCL12k that does not occur for the shorter PCL block copolymers.

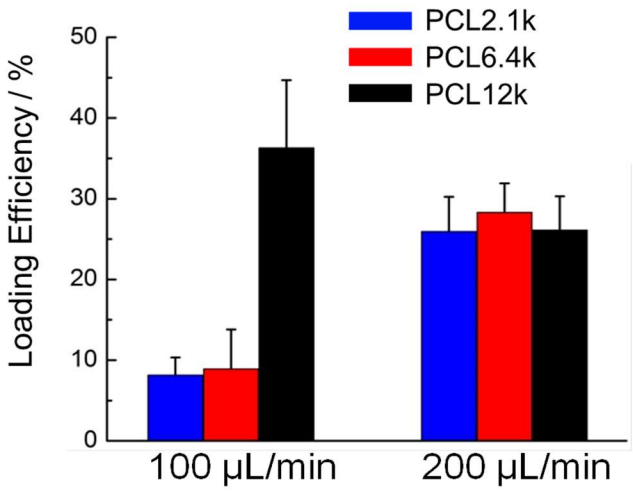

Figure 3. Effect of PCL block length on loading efficiencies of PAX-loaded PNPs prepared in the microfluidic reactor at two different flow rates and a loading ratio of r = 0.10.

Effect of Loading Ratio on Structure and Loading Efficiency of Drug Delivery PNPs. To investigate the range of structural characteristics and function accessible by microfluidic formation of drug delivery PNPs from a single copolymer, we focus on the PCL6.4k copolymer for the remainder of this study. First, we explored the effect of the initial drug : polymer ratio (w/w), r, at a constant flow rate of Q = 100 µL / min (Figure 4). Data for the r =

0.10 case (Figure 2B) is included in Figure 4 for completeness. Table 2 summarizes the resulting PNP characteristics (morphologies, hydrodynamic sphere diameters, PCL crystallinities, and loading efficiencies/levels) from triplicate preparations under each set of conditions.

Table 2. Characteristics of PAX-Loaded PNPs Described in Figure 4.[a]

r	Morphologies[b]	χ_{PCL} (%)	Loading Efficiency (%)	Loading Level[c]
0.10	S (28), C, L	11 ± 2	9 ± 3	0.009 ± 0.003
0.25	S (12), C, RC, L	10 ± 2	19 ± 3	0.048 ± 0.008
0.50	S (15), RC, L	16 ± 3	3 ± 1	0.015 ± 0.004
0.60	S (15)	7 ± 2	15 ± 7	0.09 ± 0.04

a) All samples in Table 2 prepared from PCL6.4k at Q = 100 μL / min.

b) Prominent morphologies are indicated as S (spheres), C (cylinders or filomicelles), RC (rigid cylinders), V (vesicles), and L (lamellae). Numbers in brackets indicate peak hydrodynamic diameters (in nm) of spheres (assumed to be smallest-sized population) from CONTIN analysis.

c) Calculated from *loading level* = (*r* × *loading efficiency*) / 100

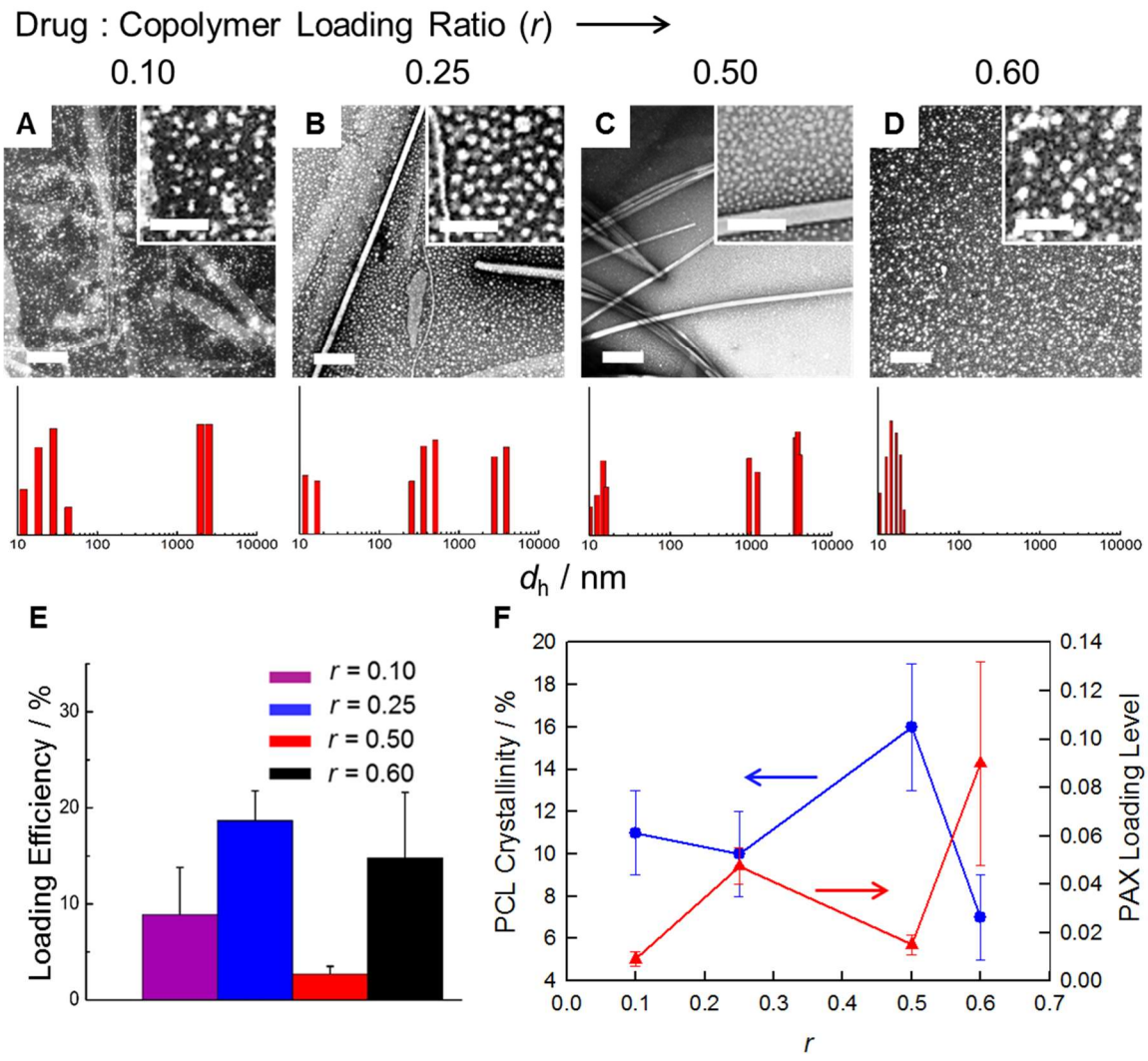

Figure 4. Effect of loading ratio on morphologies, sizes, loading efficiencies and PCL crystallinities of PAX-loaded PNPs prepared in the microfluidic reactor. Representative TEM images and DLS CONTIN size distributions (A-D), loading efficiencies (E), and PCL crystallinities and PAX loading levels (F) for PNPs formed from PCL6.4k at a flow rate of Q = 100 μL / min. All scale bars are 200 nm.

Figure 4, A-D shows representative TEM images and associated intensity-weighted DLS hydrodynamic size distributions of PAX-loaded PNPs formed at Q = 100 μL / min from PCL6.4k with increasing loading ratios from left to right of r = 0.10 (A), 0.25 (B), 0.50 (C), 0.60 (D). All conditions form similar populations of small spheres, as shown in the TEM insets and from the

smaller-sized population in the DLS distributions. The larger morphologies change significantly as the amount of added PAX increases from r = 0.1 to r = 0.5 (Figure 4, A-C), then disappear completely at the highest loading ratio of r = 0.6 (Figure 4D). The increased predominance of rigid cylinders between r = 0.1 (Figure 4A) and r = 0.5 (Figure 4C) corresponds to an initial increase in the crystallinity of the PCL cores as more PAX is added (Figure 4E). We attribute these trends to the possible role of PAX as a plasticizer within the PCL core, which increases the rate of crystallite growth and promotes the formation of rigid cylinders.[49,50] Both trends reverse at the highest amount of added PAX, r = 0.60, where the larger morphologies disappear completely (Figure 4D) and the PCL crystallinity drops sharply (Figure 4E).

PAX loading efficiencies (Figure 4E) and hence loading levels (Figure 4F, red plot) do not follow a monotonic trend with increasing r, but rather track closely with PCL crystallinity (Figure 4F, blue plot): that is, as the PCL crystallinity increases between r = 0.25 and r = 0.50, the loading level decreases, and then increases when the PCL crystallinity drops sharply between r = 0.50 and r = 0.60 (Figure 4F). This remarkable correlation underlines the role of PCL crystallization in excluding PAX and other hydrophobic cargo from the PNP cores. It also suggests that, at constant flow rate, the amount of added drug can have a significant effect on the crystallinity and hence the loading efficiency, in some cases even leading to decreases in the loading level (encapsulated drug : polymer w/w) as the loading ratio (added drug : polymer w/w) increases, as is found between r = 0.25 and r = 0.50 in Figure 4E.

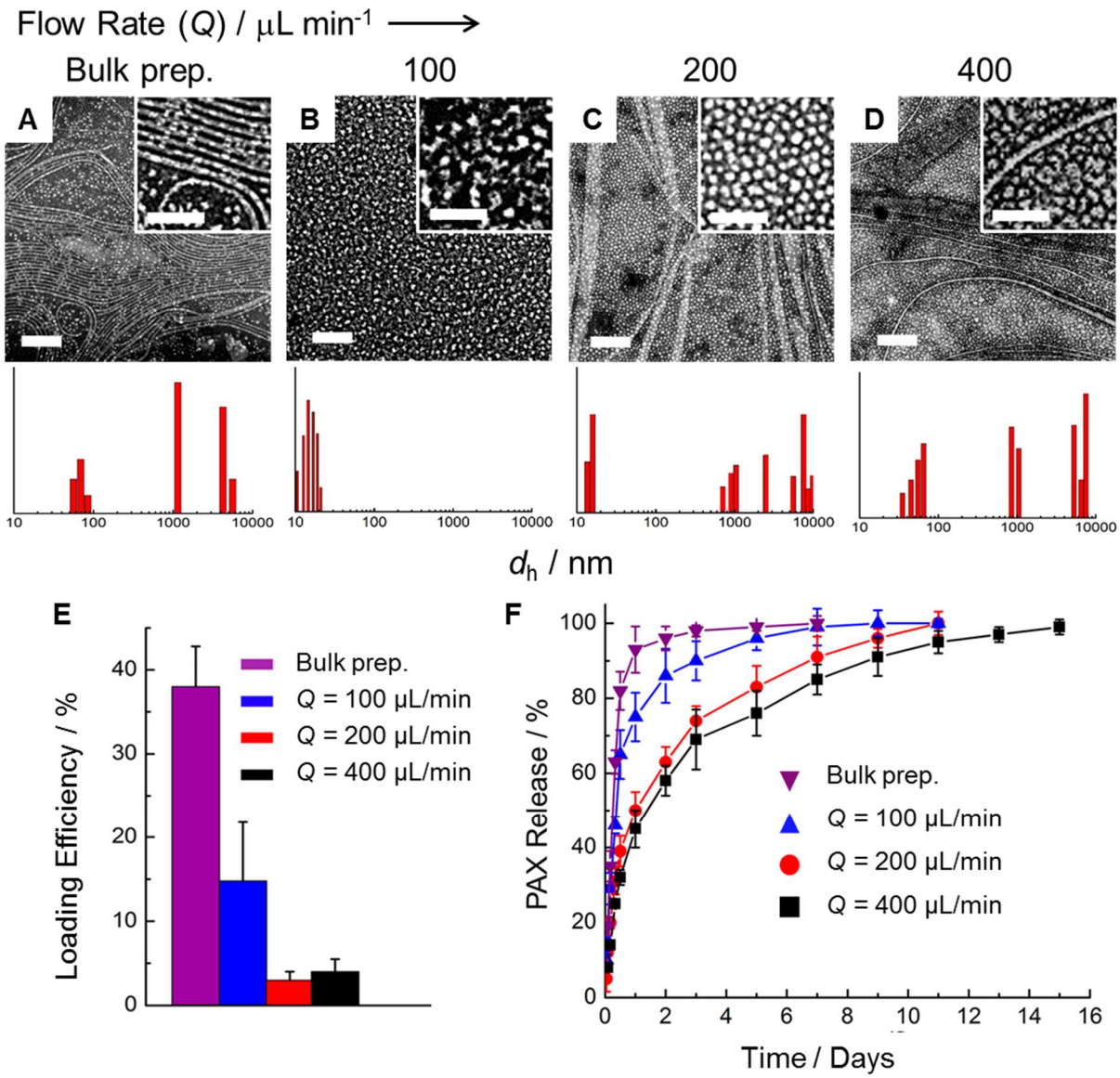

Figure 5. Effect of preparation method and flow rate on morphologies, sizes, loading efficiencies, and *in vitro* release profiles of PAX-loaded PNPs. Representative TEM images and DLS CONTIN size distributions (A-D), loading efficiencies (E), and *in vitro* release profiles (F) for PNPs formed from PCL6.4k by the bulk method and in the microfluidic reactor at different flow rates. For these experiments, the loading ratio was $r = 0.60$. All scale bars are 200 nm.

Effect of Flow Rate on Structure and Function of Microfluidic-Prepared Drug Delivery PNPs. The previous sections demonstrated that chemical parameters, including PCL block length and amount of added PAX, are important factors affecting the structure and loading

of drug delivery PNPs prepared using microfluidics, as they have shown to be in conventional manufacturing methods. In this section, we demonstrate flow-variable shear processing on the structure and function of microfluidic-prepared PNPs prepared from PCL6.4k at the highest investigated PAX loading ratio, r = 0.60. Figure 5 presents morphologies, sizes, loading efficiencies, and release profiles of PNPs prepared at three different flow rates (Q = 100, 200 and 400 μL / min) and by conventional drop-wise water addition (bulk preparation). Data for the Q = 100 μL / min case (Figure 4D) are included in Figure 5 for completeness. The resulting PNPs were also compared in cell viability assays (growth inhibition) against the MCF-7 breast cancer cell line (Figure 6). Table 3 summarizes the resulting shear-variable characteristics for each PNP preparation (morphologies, hydrodynamic sphere diameters, loading efficiency/level, PAX release half time, $t_{1/2}$, and PAX concentration for 50 % MCF-7 growth inhibition, GI_{50}) from triplicate preparations.

Table 3. Structure and Drug Delivery Characteristics of Bulk and Flow-Variable Microfluidic-Prepared PAX-Loaded PNPs Described in Figures 5 and 6.[a]

Q (μL/min)	Morphologies[b]	Loading Efficiency (%)	$\tau_{1/2}$ (hours)	Incubation Time (hours)	GI_{50} ($\times 10^3$ μg/mL)
Bulk	S (69), C, L	38 ± 5	7	48	0.8 ± 0.1
				72	3.0 ± 0.4
				96	3.0 ± 0.6
100	S (15)	15 ± 7	14	48	1.5 ± 0.4
				72	4 ± 1
				96	11 ± 6
200	S (16), C, L	3 ± 1	24	48	0.20 ± 0.06
				72	0.6 ± 0.1
				96	3.1 ± 0.7
400	S (65), C, L	4 ± 2	35	48	3.1 ± 0.3
				72	5 ± 1
				96	7 ± 2

a) All samples in Table 3 prepared from PCL6.4k at $r = 0.6$.

b) Prominent morphologies are indicated as S (spheres), C (cylinders or filomicelles), and L (lamellae). Numbers in brackets indicate peak hydrodynamic diameters (in nm) of spheres (assumed to be smallest-sized population) from CONTIN analysis.

Figure 5, A-D shows representative TEM images and associated intensity-weighted DLS hydrodynamic size distributions of PAX-loaded PNPs (PCL6.4k, $r = 0.60$) prepared at increasing flow rate from left to right: bulk (A), $Q = 100$ μL / min (B), $Q = 200$ μL / min (C), $Q = 400$ μL / min (D). The nonmonotonic size and morphological trends are attributed to the interplay of three competing mechanisms of PNP shear processing: 1) shear-induced particle breakup,[63,64] 2) shear-induced particle coalescence,[63,64] and 3) shear-induced polymer crystallization.[62,67,68] In the lowest-shear case of the bulk preparation (Figure 5A), a mixture of spheres, long filaments, and

lamellae are formed, with DLS showing the population of spheres to be sized at ~69 nm. Comparison of TEM and DLS results in Figure 5A with the microfluidic preparation at the lowest flow rate (Q = 100 μL / min, Figure 5B) suggests breakup of larger aggregates by shear processing under these conditions, forming a single population of roughly spherical PNPs (~15 nm by DLS). Further increasing the flow rate (Q = 200 μL / min, Figure 5C), we see a return of larger particle morphologies, including lamellae and a few filaments, suggesting shear-induced particle coalescence, shear-induced crystallization, or a combination of both mechanisms which favor the formation of large extended morphologies.[63,64,67] In addition, DLS distributions corroborated by TEM images suggest that shear processing significantly lowered the polydispersity of spheres formed at Q = 200 μL / min (Figure 5C) while maintaining their mean size relative to the Q = 100 μL / min case (Figure 5B). Finally, when the shear rate is turned up further by increasing the flow rate to Q = 400 μL / min, we see an increase in the predominance of long filaments along with an increase in the size and polydispersity of spheres, possibly due to shear-coalescence of smaller spheres, breakdown of large lamellae, or a combination of both mechanisms.

The TEM and DLS results described above demonstrate that simple variation of flow rate in the microfluidic channels allows modulation of important structural features germane to biological transport, targeting, and cellular uptake.[11,42,43,45,47] First, shear-directed tuning of PNP sizes with changes in flow rate (e.g. Figure 5, C and D) is shown in the critical size regime between 10 nm and 100 nm, where PNPs are small enough to avoid opsonization but large enough not be cleared by the renal and lymphatic systems.[11] Such facile tuning of sizes *via* flow rate in this regime could be a critical tool for optimizing both enhanced permeability and retention (EPR) and cellular uptake for specific cancer therapies, both size-dependent processes

which are also highly variable with different tumor and cell types.[11,41] Second, along with the importance of tuning mean size, lowering size dispersities by shear processing (e.g. Figure 5, B and D) could ensure a maximize number of PNPs in a formulation arriving at the therapeutic target.[46] Finally, we show that shear processing provides pathways to generating specific extended morphologies, including lamellae (Figure 5C) and filaments (Figure 5D); such extended morphologies have been shown to exhibit desirable therapeutic properties, including longer circulation times, higher drug loading, and gradual hydrolytic breakdown into smaller PNPs amenable to cell uptake.[16,31,42,43]

PAX loading efficiencies for preparation conditions represented in Figure 5, A-D are shown in Figure 5E. The bulk preparation shows the highest loading efficiency, followed by the microfluidic PNPs prepared at Q = 100 μL / min. Loading efficiency decreases further with an increase in flow rate to Q = 200 μL / min but remains relatively constant (within error) when the flow rate is increased to Q = 400 μL / min. The high loading efficiency of the bulk preparation is attributed to a combination of the large number of filaments with extended hydrophobic cores (Figure 5A) along with kinetic effects arising from dropwise water addition; as water is added slowly, the PCL cores will be highly swollen with solvent, allowing a high concentration of PAX to diffuse into the dynamic cores before crystallization and kinetic trapping occurs. In contrast, fast microfluidic mixing and smaller PCL cores (Figure 5B) lead to a drop in loading efficiency at Q = 100 μL / min relative to the bulk preparation. The further drop in loading efficiency when the flow rate is increased to Q = 200 μL / min may be attributed to the corresponding increase in PCL crystallinity (from 7 to 18 wt %) excluding more PAX from the PNPs. We note that this decrease in loading efficiency with increasing flow rate from Q = 100 μL / min to Q = 200 μL / min contrasts the opposite trend described earlier for the same copolymer (PCL6.4k) at a lower

loading ratio of $r = 0.10$ (Figure 3); this underlines that microfluidic flow dependencies provide a useful experimental handle on PNP structure and function, although specific flow effects can be highly dependent on the chemical properties of a given formulation.

In vitro PAX release profiles (Figure 5F) show that the bulk preparation exhibits unfavorably fast release in contrast to microfluidic-prepared PNPs. The bulk sample (purple) shows mainly burst release with >90 % PAX released after 1 day suggesting that, despite a high encapsulation efficiency (Figure 5E), the encapsulated drug was localized at or near the core-corona interface. Microfluidic PNPs prepared at Q = 100 μL / min (blue) show significantly slower release, with ~75 % of the drug released after 1 day and complete release after 7 days. We attribute slower release of microfluidic-prepared PNPs to fast mixing giving rise to more homogenous distributions of PAX within the core. Moreover, we find PNP release profiles can be further extended by forming PNPs at increased flow rates of Q = 200 μL / min (red) or Q = 400 μL / min (black), which result in extended release over 11 and 15 days, respectively. At these higher flow rates, shear-induced crystallization may play a role in further slowing rates of PAX diffusion rates out of the core.[67]

Antiproliferative effects for each of the PNP preparations from Figure 5 were measured using the MCF-7 cell line. Free PAX was evaluated as a positive control and empty PNPs (no PAX) of PCL2.1k (similar chemistry and colloidal structures to PCL6.4k, e.g. Figure 2) were evaluated as a negative control. For all investigated samples and controls, growth inhibition was determined for 48 h, 72 h, and 96 h incubation times (Supporting Information, Figures S2-S4). Negative controls suggest no significant effect of empty PNPs on cell proliferation, showing negligible growth inhibition up to a highest investigated polymer concentration of 750 ppm

(Supporting Information, Figure S5), which is orders of magnitude above the highest polymer concentration applied in doses of PAX-loaded PNPs (1.65 ppm).

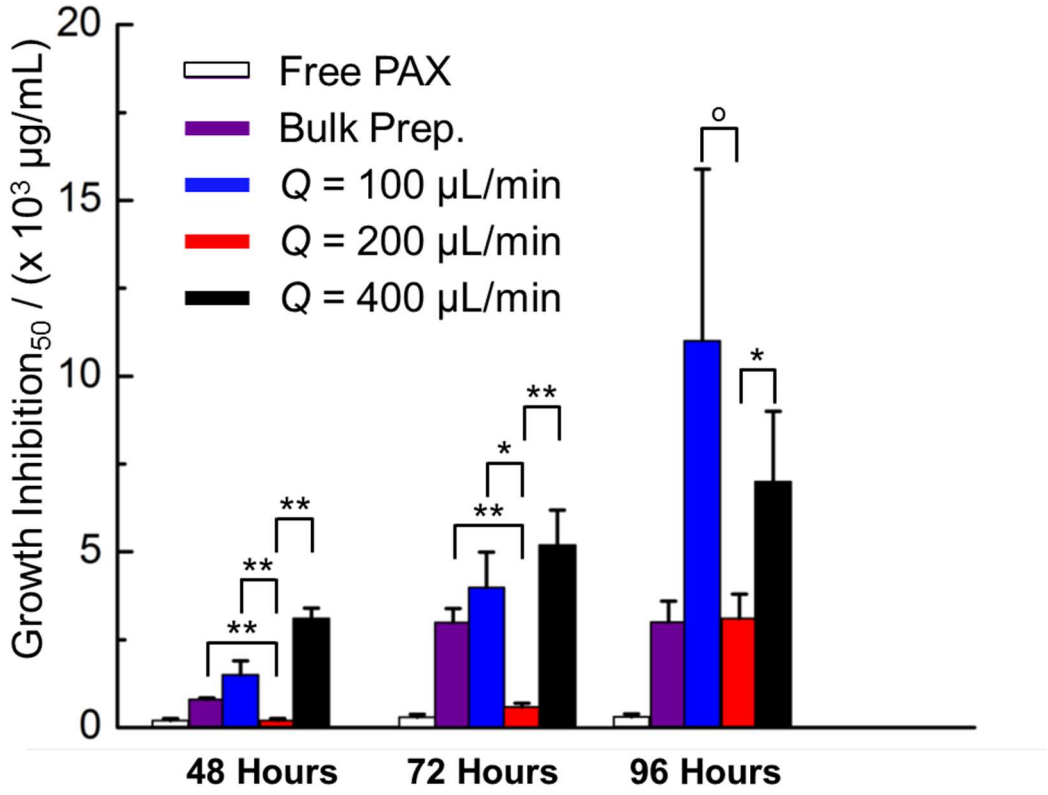

Figure 6. Effect of preparation method and flow rate on MCF-7 antiproliferation potency (GI_{50} values) for PAX-loaded PNPs prepared from PCL6.4k at a loading ratio of r = 0.60. Data is shown for incubation times of 48 h, 72 h, and 96 h. Connecting brackets indicate statistical comparisons between microfluidic-prepared PNPs generated at an intermediate flow rate (Q = 200 µL/min) and PNPs generated under other conditions. Single asterisks indicate $p < 0.05$; double asterisks indicate $p < 0.01$; open circles indicate $p > 0.05$.

Comparative growth inhibition plots (Figure S1) and associated GI_{50} values in Figure 6 reveal significant differences in antiproliferative effects for different preparations of PAX-loaded PNPs. Considering the 48 h data, most of the PNP formulations show attenuated antiproliferative effects (elevated GI_{50} values) relative to free PAX, a probable result of cells not being fully exposed to encapsulated drug. We find that for all but one sample, GI_{50} values increase as the

associated PNP release rates decrease (Figure 5F). The marked exception is the microfluidic Q = 200 μL / min formulation which, despite having the second-slowest PAX release in PBS buffer (Figure 5F), showed the greatest potency (GI_{50} = 0.2 × 10^{-3} μg/mL) among the PNP samples, identical to that determined for free PAX. Compared to the Q = 400 μL / min preparation, PNPs formed at Q = 200 μL / min possess similar PAX loading levels (Figure 5E) and release rates (Figure 5F) and so neither of these characteristics can be responsible for the significantly lower GI_{50} of the latter preparation. We tentatively attribute the enhanced potency of the Q = 200 μL / min sample to the specific shear-directed structure of the PNPs formed in the microfluidic channels at this flow rate (Figure 5C). Although the presence of lamellae and cylinders may be involved in attenuating cell growth, we attribute the markedly stronger antiproliferative effects of the Q = 200 μL / min sample to its population of small and low-polydispersity spheres being particularly amenable to cellular interactions.[11,41]

GI_{50} values for all PAX formulations increased with incubation time (Figure 6) since more numerous cells at longer incubation times require higher PAX doses to deplete their growth. For 72 h incubation, the Q = 200 μL / min microfluidic preparation continues to show the lowest GI_{50} values of the PNP formulations; for 96 h incubation, both the bulk preparation and Q = 200 μL / min microfluidic preparation show equivalently low GI_{50} values. These data indicate that flow-tunable processing and structural control of PNPs prepared in the microfluidic reactor can provide routes to optimized antiproliferative effects that are stronger than those from conventional bulk PNP preparation methods. Another intriguing possibility is that tuning of structure-dependent cellular interactions *via* microfluidic shear processing could lead to more selective PNP cytotoxicity for cancer cells relative to normal cells, an application that will be discussed in a future publication.

Conclusions

We have demonstrated control of multiscale structure and drug delivery function for PAX-loaded PCL-*b*-PEO PNPs *via* synthesis and flow-directed shear processing in a two-phase gas-liquid microfluidic reactor. For the lowest investigated drug : polymer ratio (w/w), $r = 0.1$, PNPs formed at two different flow rates (Q = 100 μL / min and 200 μL / min) showed flow-variable sizes and morphologies that depended on the length of the PCL block. For all three PCL block lengths, the higher flow rate resulted in sphere populations becoming less polydisperse with accompanying larger morphologies (e.g. filaments, vesicles) forming that were not present at the lower flow rate; PAX loading efficiencies were higher at the higher flow rate for all but the longest PCL block. For the middle PCL block length (PCL6.4k) we investigated effects of loading ratio (at Q = 100 μL / min) and flow rate (at $r = 0.60$) on PNP structure and function. As the loading ratio of PAX increased from $r = 0.1$ to $r = 0.6$ at constant flow rate, we found nonmonotonic trends in morphology, crystallinity, and loading efficiency, as PAX addition first promoted ($r = 0.1 – 0.5$) then attenuated ($r = 0.6$) PCL crystallization. Finally, by varying microfluidic flow rate from Q = 100 μL / min to Q = 400 μL / min and comparing with a conventional bulk method of PNP preparation, we showed that flow-variable shear processing enabled tunable PNP sizes/morphologies and increased release times (up to 2 weeks) with increasing flow rate. Moreover, antiproliferative effects against cultured MCF-7 breast cancer cells were greatest for PNPs formed at the intermediate microfluidic flow rate, Q = 200 μL / min, corresponding to the small and low-polydispersity spheres formed uniquely at this condition. Overall, these results demonstrate that formation and flow-directed nanoscale shear processing in gas-liquid microfluidic reactors provides a manufacturing platform for PNPs that could enable more effective and selective nanomedicines through multiscale structural control.

Supporting Information. Critical water content data and discussion; tables of actual flow rates; prepresentative MCF-7 antiproliferative data for PAX-loaded and empty (control) PNPs; additional TEM images.

Acknowledgements. We are grateful to the Natural Sciences and Engineering Research Council of Canada, NSERC, for financial support. We acknowledge Dr. Patrick Nahirney and the UVic EM lab (Department of Biology) for the continued use of their TEM.

References

(1) Allen, C.; Maysinger, D.; Eisenberg, A. Nano-engineering block copolymer aggregates for drug delivery. *Colloids and Surfaces B: Biointerfaces* **1999**, *16*, 3-27.

(2) Discher, D. E.; Ortiz, V.; Srinivas, G.; Klein, M. L.; Kim, Y.; Christian, D.; Cai, S.; Photos, P.; Ahmed, F. Emerging Applications of Polymersomes in Delivery: from Molecular Dynamics to Shrinkage of Tumors. *Prog Polym Sci* **2007**, *32*, 838-857.

(3) Branco, M. C.; Schneider, J. P. Self-assembling materials for therapeutic delivery. *Acta biomaterialia* **2009**, *5*, 817-831.

(4) Tyrrell, Z. L.; Shen, Y. Q.; Radosz, M. Fabrication of micellar nanoparticles for drug delivery through the self-assembly of block copolymers. *Prog Polym Sci* **2010**, *35*, 1128-1143.

(5) Gong, J.; Chen, M. W.; Zheng, Y.; Wang, S. P.; Wang, Y. T. Polymeric micelles drug delivery system in oncology. *Journal of Controlled Release* **2012**, *159*, 312-323.

(6) Kataoka, K.; Harada, A.; Nagasaki, Y. Block copolymer micelles for drug delivery: Design, characterization and biological significance. *Adv Drug Deliver Rev* **2012**, *64*, 37-48.

(7) Parveen, S.; Misra, R.; Sahoo, S. K. Nanoparticles: a boon to drug delivery, therapeutics, diagnostics and imaging. *Nanomed-Nanotechnol* **2012**, *8*, 147-166.

(8) Lee, J. S.; Feijen, J. Polymersomes for drug delivery: Design, formation and characterization. *Journal of Controlled Release* **2012**, *161*, 473-483.

(9) Kwon, G. S.; Kataoka, K. Block copolymer micelles as long-circulating drug vehicles. *Adv Drug Deliver Rev* **2012**, *64*, 237-245.

(10) Rosler, A.; Vandermeulen, G. W. M.; Klok, H. A. Advanced drug delivery devices via self-assembly of amphiphilic block copolymers. *Adv Drug Deliver Rev* **2012**, *64*, 270-279.

(11) Elsabahy, M.; Wooley, K. L. Design of polymeric nanoparticles for biomedical delivery applications. *Chemical Society Reviews* **2012**, *41*, 2545-2561.

(12) Zhang, Y.; Chan, H. F.; Leong, K. W. Advanced materials and processing for drug delivery: The past and the future. *Adv Drug Deliver Rev* **2013**, *65*, 104-120.

(13) Nicolas, J.; Mura, S.; Brambilla, D.; Mackiewicz, N.; Couvreur, P. Design, functionalization strategies and biomedical applications of targeted biodegradable/biocompatible polymer-based nanocarriers for drug delivery. *Chemical Society Reviews* **2013**, *42*, 1147-1235.

(14) Lu, Y.; Park, K. Polymeric micelles and alternative nanonized delivery vehicles for poorly soluble drugs. *Int J Pharmaceut* **2013**, *453*, 198-214.

(15) Ahmad, Z.; Shah, A.; Siddiq, M.; Kraatz, H. B. Polymeric micelles as drug delivery vehicles. *Rsc Adv* **2014**, *4*, 17028-17038.

(16) Oltra, N. S.; Nair, P.; Discher, D. E. From Stealthy Polymersomes and Filomicelles to "Self" Peptide-Nanoparticles for Cancer Therapy. *Annu Rev Chem Biomol* **2014**, *5*, 281-299.

(17) Sun, T.; Zhang, Y. S.; Pang, B.; Hyun, D. C.; Yang, M.; Xia, Y. Engineered nanoparticles for drug delivery in cancer therapy. *Angewandte Chemie International Edition* **2014**, *53*, 12320-12364.

(18) Yokoyama, M. Polymeric micelles as drug carriers: their lights and shadows. *Journal of drug targeting* **2014**, *22*, 576-583.

(19) Prabhu, R. H.; Patravale, V. B.; Joshi, M. D. Polymeric nanoparticles for targeted treatment in oncology: current insights. *Int J Nanomed* **2015**, *10*, 1001-1018.

(20) Ulbrich, K.; Hola, K.; Subr, V.; Bakandritsos, A.; Tucek, J.; Zboril, R. Targeted Drug Delivery with Polymers and Magnetic Nanoparticles: Covalent and Noncovalent Approaches, Release Control, and Clinical Studies. *Chem Rev* **2016**, *116*, 5338-5431.

(21) Lee, S. C.; Kim, C.; Kwon, I. C.; Chung, H.; Jeong, S. Y. Polymeric micelles of poly(2-ethyl-2-oxazoline)-block-poly(epsilon-caprolactone) copolymer as a carrier for paclitaxel. *Journal of Controlled Release* **2003**, *89*, 437-446.

(22) Ahmed, F.; Discher, D. E. Self-porating polymersomes of PEG-PLA and PEG-PCL: hydrolysis-triggered controlled release vesicles. *Journal of controlled release : official journal of the Controlled Release Society* **2004**, *96*, 37-53.

(23) Ahmed, F.; Pakunlu, R. I.; Brannan, A.; Bates, F. S.; Minko, T.; Discher, D. E. *J. Control. Release* **2006**, *116*, 150.

(24) Zupancich, J. A.; Bates, F. S.; Hillmyer, M. A. Aqueous dispersions of poly(ethylene oxide)-b-poly(gamma-methyl-epsilon-caprolactone) block copolymers. *Macromolecules* **2006**, *39*, 4286-4288.

(25) Locatelli, E.; Franchini, M. C. Biodegradable PLGA-b-PEG polymeric nanoparticles: synthesis, properties, and nanomedical applications as drug delivery system. *J Nanopart Res* **2012**, *14*.

(26) Zhang, K. R.; Tang, X.; Zhang, J.; Lu, W.; Lin, X.; Zhang, Y.; Tian, B.; Yang, H.; He, H. B. PEG-PLGA copolymers: Their structure and structure-influenced drug delivery applications. *Journal of Controlled Release* **2014**, *183*, 77-86.

(27) Allen, C.; Yu, Y. S.; Maysinger, D.; Eisenberg, A. *Bioconjugate Chem.* **1998**, *9*, 564-572.

(28) Allen, C.; Yu, Y. S.; Eisenberg, A.; Maysinger, D. Cellular internalization of PCL20-b-PEO44 block copolymer micelles. *Bba-Biomembranes* **1999**, *1421*, 32-38.

(29) Allen, C.; Han, J. N.; Yu, Y. S.; Maysinger, D.; Eisenberg, A. Polycaprolactone-b-poly(ethylene oxide) copolymer micelles as a delivery vehicle for dihydrotestosterone. *Journal of Controlled Release* **2000**, *63*, 275-286.

(30) Lim Soo, P.; Luo, L.; Maysinger, D.; Eisenberg, A. *Langmuir* **2002**, *18*, 9996-10004.

(31) Geng, Y.; Discher, D. E. Hydrolytic degradation of poly(ethylene oxide)-block-polycaprolactone worm micelles. *J Am Chem Soc* **2005**, *127*, 12780-12781.

(32) Ghoroghchian, P. P.; Li, G.; Levine, D. H.; Davis, K. P.; Bates, F. S.; Hammer, D. A.; Therien, M. J. Bioresorbable Vesicles Formed through Spontaneous Self-Assembly of Amphiphilic Poly(ethylene oxide)-block-polycaprolactone. *Macromolecules* **2006**, *39*, 1673-1675.

(33) Letchford, K.; Liggins, R.; Wasan, K.; Burt, H. In vitro human plasma distribution of nanoparticulate paclitaxel is dependent on the physicochemical properties of poly(ethylene glycol)-block-poly(caprolactone) nanoparticles. *Eur J Pharm Biopharm* **2009**, *71*, 196-206.

(34) Ostacolo, L.; Marra, M.; Ungaro, F.; Zappavigna, S.; Maglio, G.; Quaglia, F.; Abbruzzese, A.; Caraglia, M. In vitro anticancer activity of docetaxel-loaded micelles based on poly(ethylene oxide)-poly(epsilon-caprolactone) block copolymers: Do nanocarrier properties have a role? *Journal of Controlled Release* **2010**, *148*, 255-263.

(35) Letchford, K.; Burt, H. M. Copolymer micelles and nanospheres with different in vitro stability demonstrate similar paclitaxel pharmacokinetics. *Mol Pharm* **2012**, *9*, 248-260.

(36) Glover, A. L.; Nikles, S. M.; Nikles, J. A.; Brazel, C. S.; Nikles, D. E. Polymer micelles with crystalline cores for thermally triggered release. *Langmuir* **2012**, *28*, 10653-10660.

(37) Chang, L. L.; Wang, W. W.; Huang, P. S.; Lv, Z. S.; Hu, F. Q.; Zhang, J. H.; Kong, D. L.; Deng, L. D.; Dong, A. J. Photo-crosslinked poly(ethylene glycol)-b-poly(epsilon-caprolactone) nanoparticles for controllable paclitaxel release. *J Biomat Sci-Polym E* **2013**, *24*, 1900-1921.

(38) Park, E. K.; Kim, S. Y.; Lee, S. B.; Lee, Y. M. Folate-conjugated methoxy poly(ethylene glycol)/poly(epsilon-caprolactone) amphiphilic block copolymeric micelles for tumor-targeted drug delivery. *Journal of Controlled Release* **2005**, *109*, 158-168.

(39) Jiang, J.; Tong, X.; Zhao, Y. A new design for light-breakable polymer micelles. *J Am Chem Soc* **2005**, *127*, 8290-8291.

(40) Jiang, J. Q.; Tong, X.; Morris, D.; Zhao, Y. Toward photocontrolled release using light-dissociable block copolymer micelles. *Macromolecules* **2006**, *39*, 4633-4640.

(41) Blanco, E.; Shen, H.; Ferrari, M. Principles of nanoparticle design for overcoming biological barriers to drug delivery. *Nat Biotechnol* **2015**, *33*, 941-951.

(42) Cai, S.; Vijayan, K.; Cheng, D.; Lima, E. M.; Discher, D. E. Micelles of different morphologies--advantages of worm-like filomicelles of PEO-PCL in paclitaxel delivery. *Pharmaceutical research* **2007**, *24*, 2099-2109.

(43) Geng, Y.; Dalhaimer, P.; Cai, S.; Tsai, R.; Tewari, M.; Minko, T.; Discher, D. E. Shape effects of filaments versus spherical particles in flow and drug delivery. *Nat Nanotechnol* **2007**, *2*, 249-255.

(44) Fairley, N.; Hoang, B.; Allen, C. Morphological Control of Poly(ethylene glycol)-block-poly(eta-caprolactone) Copolymer Aggregates in Aqueous Solution. *Biomacromolecules* **2008**, *8*, 2283-2291.

(45) Venkataraman, S.; Hedrick, J.; Ong, Z.; Yang, C.; Ee, P.; Hammond, P.; Yang, Y. The effects of polymeric nanostructure shape on drug delivery. *Adv Drug Deliver Rev* **2011**, *63*, 1228-1246.

(46) Gaumet, M.; Vargas, A.; Gurny, R.; Delie, F. Nanoparticles for drug delivery: The need for precision in reporting particle size parameters. *Eur J Pharm Biopharm* **2008**, *69*, 1-9.

(47) Truong, N. P.; Whittaker, M. R.; Mak, C. W.; Davis, T. P. The importance of nanoparticle shape in cancer drug delivery. *Expert Opin Drug Del* **2015**, *12*, 129-142.

(48) Du, Z. X.; Xu, J. T.; Fan, Z. Q. Micellar morphologies of poly(epsilon-caprolactone)-b-poly(ethylene oxide) block copolymers in water with a crystalline core. *Macromolecules* **2007**, *40*, 7633-7637.

(49) Du, Z. X.; Xu, J. T.; Fan, Z. Q. Regulation of micellar morphology of PCL-b-PEO block copolymers by crystallization temperature. *Macromol Rapid Comm* **2008**, *29*, 467-471.

(50) Rizis, G.; van de Ven, T. G. M.; Eisenberg, A. Crystallinity-driven morphological ripening processes for poly(ethylene oxide)-block-polycaprolactone micelles in water. *Soft Matter* **2014**, *10*, 2825-2835.

(51) Zhang, L.; Eisenberg, A. Multiple Morphologies of "Crew-Cut" Aggregates of Polystyrene-b-poly(acrylic acid) Block Copolymers. *Science* **1995**, *268*, 1728-1731.

(52) Zhang, L.; Eisenberg, A. Multiple Morphologies and Characteristics of "Crew-Cut" Micelle-like Aggregates of Polystyrene-b-poly(acrylic acid) Diblock Copolymers in Aqueous Solutions. *J Am Chem Soc* **1996**, *118*, 3168-3181.

(53) Yu, Y. S.; Eisenberg, A. Control of morphology through polymer-solvent interactions in crew-cut aggregates of amphiphilic block copolymers. *J Am Chem Soc* **1997**, *119*, 8383-8384.

(54) Zhang, L.; Yu, K.; Eisenberg, A. Ion-Induced Morphological Changes in ``Crew-Cut" Aggregates of Amphiphilic Block Copolymers. *Science* **1996**, *272*, 1777-1779.

(55) Zhang, L. E., A. Morphogenic Effect of Added Ions on Crew-Cut Aggregates of Polystyrene-b-poly(acrylic acid) Block Copolymers in Solutions. *Macromolecules* **1996**, *29*, 8805-8815.

(56) Schabas, G.; Wang, C. W.; Oskooei, A.; Yusuf, H.; Moffitt, M. G.; Sinton, D. Formation and shear-induced processing of quantum dot colloidal assemblies in a multiphase microfluidic chip. *Langmuir* **2008**, *24*, 10596-10603.

(57) Wang, C. W.; Oskooei, A.; Sinton, D.; Moffitt, M. G. Controlled Self-Assembly of Quantum Dot-Block Copolymer Colloids in Multiphase Microfluidic Reactors. *Langmuir* **2010**, *26*, 716-723.

(58) Bawn, C.: Encyclopedia of polymer science and engineering: JI Kroschwitz, HF Mark, N. Bikales, CG Overberger and G. Menges (eds.) John Wiley and Sons, New York, 1985, 906 pages, US $240,£ 170, ISBN 0-471-89540-7. Elsevier, 1987.

(59) Karnik, R.; Gu, F.; Basto, P.; Cannizzaro, C.; Dean, L.; Kyei-Manu, W.; Langer, R.; Farokhzad, O. C. Microfluidic platform for controlled synthesis of polymeric nanoparticles. *Nano Lett* **2008**, *8*, 2906-2912.

(60) Xu, Q. B.; Hashimoto, M.; Dang, T. T.; Hoare, T.; Kohane, D. S.; Whitesides, G. M.; Langer, R.; Anderson, D. G. Preparation of Monodisperse Biodegradable Polymer Microparticles Using a Microfluidic Flow-Focusing Device for Controlled Drug Delivery. *Small* **2009**, *5*, 1575-1581.

(61) Capretto, L.; Carugo, D.; Mazzitelli, S.; Nastruzzi, C.; Zhang, X. L. Microfluidic and lab-on-a-chip preparation routes for organic nanoparticles and vesicular systems for nanomedicine applications. *Adv Drug Deliver Rev* **2013**, *65*, 1496-1532.

(62) Xu, Z. Q.; Lu, C. H.; Riordon, J.; Sinton, D.; Moffitt, M. G. Microfluidic Manufacturing of Polymeric Nanoparticles: Comparing Flow Control of Multiscale Structure in Single-Phase Staggered Herringbone and Two-Phase Reactors. *Langmuir* **2016**, *32*, 12781-12789.

(63) Wang, C. W.; Sinton, D.; Moffitt, M. G. Flow-Directed Block Copolymer Micelle Morphologies via Microfluidic Self-Assembly. *J Am Chem Soc* **2011**, *133*, 18853-18864.

(64) Wang, C. W.; Sinton, D.; Moffitt, M. G. Morphological Control via Chemical and Shear Forces in Block Copolymer Self-Assembly in the Lab-on-Chip. *Acs Nano* **2013**, *7*, 1424-1436.

(65) Wang, C. W.; Bains, A.; Sinton, D.; Moffitt, M. G. Flow-Directed Assembly of Block Copolymer Vesicles in the Lab-on-a-Chip. *Langmuir* **2012**, *28*, 15756-15761.

(66) Xu, Z. Q.; Yan, B.; Riordon, J.; Zhao, Y.; Sinton, D.; Moffitt, M. G. Microfluidic Synthesis of Photoresponsive Spool-Like Block Copolymer Nanoparticles: Flow-Directed Formation and Light-Triggered Dissociation. *Chem Mater* **2015**, *27*, 8094-8104.

(67) Bains, A.; Cao, Y. M.; Moffitt, M. G. Multiscale Control of Hierarchical Structure in Crystalline Block Copolymer Nanoparticles Using Microfluidics. *Macromol Rapid Comm* **2015**, *36*, 2000-2005.

(68) Bains, A.; Wulff, J. E.; Moffitt, M. G. Microfluidic synthesis of dye-loaded polycaprolactone-block-poly (ethylene oxide) nanoparticles: Insights into flow-directed loading and in vitro release for drug delivery. *J Colloid Interf Sci* **2016**, *475*, 136-148.